materials

MDPI

Review

Crystal Structure Formation of $CH_3NH_3PbI_{3-x}Cl_x$ Perovskite

Shiqiang Luo and Walid A. Daoud *

School of Energy and Environment, City University of Hong Kong, Tat Chee Avenue, Hong Kong, China; sqluo3-c@my.cityu.edu.hk

* Correspondence: wdaoud@cityu.edu.hk; Tel.: +852-3442-4499

Academic Editor: Joshua M. Pearce

Received: 11 December 2015; Accepted: 16 February 2016; Published: 24 February 2016

Abstract: Inorganic-organic hydride perovskites bring the hope for fabricating low-cost and large-scale solar cells. At the beginning of the research, two open questions were raised: the hysteresis effect and the role of chloride. The presence of chloride significantly improves the crystallization and charge transfer property of the perovskite. However, though the long held debate over of the existence of chloride in the perovskite seems to have now come to a conclusion, no prior work has been carried out focusing on the role of chloride on the electronic performance and the crystallization of the perovskite. Furthermore, current reports on the crystal structure of the perovskite are rather confusing. This article analyzes the role of chloride in $CH_3NH_3PbI_{3-x}Cl_x$ on the crystal orientation and provides a new explanation about the (110)-oriented growth of $CH_3NH_3PbI_3$ and $CH_3NH_3PbI_{3-x}Cl_x$.

Keywords: solar cells; perovskites; X-ray diffraction; phase transitions

1. Introduction

Since the first organic-inorganic halide perovskite solar cell was reported [1], perovskites have attracted growing interest and the power conversion efficiency (PCE) has reached 20.1% [2]. It is not very common that a photovoltaic device can experience such a rapid development. While the structure of the cells evolved from sensitized meso-structure to planar structure [3], both inorganic and organic materials can be applied as electron and hole transfer materials [4]. Furthermore, by tuning the composition of the perovskite, the band gap can be easily modified [5]. Given the numerous advantages of perovskite, a clear understanding of the crystal structure is crucial and the role of chloride in the formation of $CH_3NH_3PbI_{3-x}Cl_x$ (hereafter, we use MA short for CH_3NH_3) is one of the most pressing topics.

It has been reported that the presence of chloride in the perovskite improves the uniformity of its layer [6] and results in an increase of the carriers' diffusion length from *ca.* 100 nm to over 1 μm [7]. However, the long held debate over of the existence of chloride in the perovskite seems to have now come to a conclusion. First, when synthesizing the perovskite by the one step method with precursor solution of MACl and PbI_2 (1:1 molar ratio) in anhydrous N,N-dimethylformamide (DMF), the resulting crystal is not $MAPbI_2Cl$ but a mixture of $MAPbI_3$ and $MAPbCl_3$ [8]. This provides direct evidence that chloride (Cl^-) cannot substitute iodine (I^-) in the perovskite to form a stable crystal. Then, two contradictory results were then reported. X-ray photoelectron spectroscopy (XPS) showed that the molar ratio C:N:Pb:I:Cl of the perovskite is *ca.* 1:1:1:2:1, when prepared from a precursor of MAI:$PbCl_2$ (molar ratio 3:1) [9]. On the other hand, energy dispersive X-ray (EDX) analysis showed that no Cl^- was present in the perovskite prepared from PbI_2 + MAI + MACl [10]. Noting that the XPS was unable to determine the existence of $MAPbI_2Cl$ crystal and that EDX has its detecting limitation, more precise characterizations were needed. Later on, the simultaneous Fourier transform infrared spectroscopy analysis of the expelled

gas during the decomposition of $MAPbI_{3-x}Cl_x$ showed the presence of Cl^-, angle-resolved XPS [11] and X-ray fluorescence spectroscopy (XFS) [12] not only confirmed the existence of Cl^-, but also showed that Cl^- was located at the interface between the perovskite and the electron transport TiO_2 layer, and not in the perovskite structure [11,12]. Moreover, scanning transmission microscopy-energy dispersive spectroscopy (STEM-EDS) detected no trace of Cl^- in the perovskite. Even though there is a strong Cl^- signal, no N was observed indicting the presence of only $PbCl_2$ [13]. Thus, Cl^- only appears at the interface between $MAPbI_3$ and the anode. Two more reports have further confirmed this conclusion. XPS analysis showed only weak Cl^- signal after etching the surface of $MAPbI_{3-x}Cl_x$ by a 50 nm thickness [14]. Hard X-ray photoelectron spectroscopy and fluorescence yield X-ray absorption spectroscopy showed no Cl^- at the surface of $MAPbI_{3-x}Cl_x$ with higher average concentration of Cl throughout the perovskite layer at the deep beneath [15]. Here, we refer to $MAPbI_{3-x}Cl_x$ as $MAPbI_3$ that is prepared using chloride-containing precursors. However, as the condition for depositing $MAPbI_{3-x}Cl_x$ differs, Cl^- may still remain in the resulting perovskite layer. For instance, X-ray absorption near edge structure (XANES) results showed that $x = 0.05 \pm 0.03$ Cl atoms per formula unit remain in the films after annealing at 95 °C for 120 min [16]. The results from photothermal induced resonance (PTIR) showed that the $MAPbI_{3-x}Cl_x$ film consists of a mixture of Cl-rich ($x_{local} < 0.3$) and Cl-poor phases after a mild annealing (60 °C, 60 min) and homogeneous Cl-poorer ($x_{local} < 0.06$) phase upon further annealing (110 °C) [17].

In addition, first-principles calculation results provide some good explanation. For the crystal structure, Cl^- concentration was found below 3%–4% [8] and if the Cl^- ions enter the crystal structure, they preferentially occupy the apical positions in the PbI_4X_2 octahedra [18]. For the electronic property, while the molecular orientations of $CH_3NH_3^+$ result in three times larger photocurrent response than the ferroelectric photovoltaic $BiFeO_3$, Cl^- substitution at the equatorial site induces a larger response than does substitution at the apical site [19]. Results also showed that, using Cl^- precursor can avoid forming the PbI defects [20]. Introducing Cl^- would reduce the lattice constant which can inhibit the formation of interstitial defects [21]. As excitons may be screened by collective orientational motion of the organic cations, Cl^- might hinder this motion and results in better transport properties [22]. Little difference of electronic properties was represent among orthorhombic, tetragonal and cubic phases of $MAPbI_3$ [23], however, the valance-band-maximum and conduction-band-minimum states can be mainly derived from iodine ions at some unique positions, Cl^- substitution can strengthen the unique position of the ions and result in more localized charge density [24]. Thus, lower carrier recombination rate and enhanced carrier transport ensued. For the interface, the (001) and (110) surfaces tend to favor hole injection to 2,2′,7,7′-tetrakis(*N*,*N*-di-*p*-methoxyphenylamine)-9,9′-spirobifluorene (Spiro-MeOTAD), while the (100) surface facilitates electron transfer to [6,6]-phenyl C_{61}-butyric acid methyl ester (PCBM) [25]. A better structural matching between adjacent rows of perovskite surface halides and TiO_2 under coordinated titanium may be the reason for the (110)-oriented growth of $MAPbI_{3-x}Cl_x$ and $MAPbI_3$ [26]. Interfacial Cl^- may thus further stabilize the (110) surface and modify the interface electronic structure between $MAPbI_3$ and TiO_2 [26].

Despite the absence of Cl^- in the perovskite, it still played an important role in the crystallization process. For instance, the morphology of $MAPbI_{3-x}Cl_x$ was compared with $MAPbI_3$ [27] and a model in which the Cl^- rich phase modifies the morphologies of perovskite was proposed and fit well with the results from scanning electron microscopy (SEM) [27]. In addition, the transmission electron microscopy (TEM) of freeze-dried perovskite $MAPbI_{3-x}Cl_x$ precursor solution showed the presence of $PbCl_2$ nanoparticles [28] and this is in agreement with the dynamic light scattering (DLS) investigations of $MAPbI_{3-x}Cl_x$ precursor solution [29]. Thus, references [28,29] further proved the model of the heterogeneous nucleation by $PbCl_2$ nanoparticles proposed in reference [27]. However, the formation mechanism of the crystal structure remains undermined and this will be discussed in the following parts of this article.

2. Methods for Fabricating $MAPbI_{3-x}Cl_x$

In Section 3, we discuss the crystal structure of $MAPbI_{3-x}Cl_x$ according to the deposition method. As the fabrication methods were discussed in detail in reference [30], here we add a brief introduction

about the preparation methods of $MAPbI_{3-x}Cl_x$. For the one-step deposition method, MAI:PbI_2/$PbCl_2$ (molar ratio 1:1 or 3:1) [31,32] were dissolved in γ-butyrolactone (GBL) or DMF, spin-coated on the substrates and annealed to form perovskite. Different annealing conditions result in different morphology of the $MAPbI_{3-x}Cl_x$ layer. While a rapid thermal annealing at 130 °C resulted in micron-sized perovskite grains [33], two-step annealing, such as 90 °C for 30 min then at 100 °C for 2 min [34] or 60 °C then ramping to 90 °C [35], resulted in optimal PCE on poly(3,4-ethylenedioxythiophene) poly(styrene-sulfonate) (PEDOT:PSS) substrates. A full coverage of perovskite can be achieved by rapid cooling after annealing [36]. To increase the solubility of Cl^-, 1,8-diiodooctane [37] or other alkyl halide additives [38] or dimethyl sulfoxide [9] can be employed. Adding poly-(vinylpyrrolidone) (PVP) can also improve the surface coverage of perovskite [39]. It is interesting to note that, for $MAPbI_{3-x}Cl_x$, a simple annealing step is enough to form a good coverage [6,40], but for $MAPbI_3$, a special step, such as multi-deposition [41], adding N-cyclohexyl-2-pyrrolidone (CHP) [42], fast deposition [43–45], or air flow during spin coating [46,47], is needed.

The sequential deposition method was mainly applied for $MAPbI_3$ perovskite. In a typical synthesis, the solution of PbI_2 in DMF was spun on a substrate as the first step then the substrate was dipped in a solution of MAI in 2-propanol (IPA) to form $MAPbI_3$ crystals as the second step [48]. For the inclusion of chloride, in the first step the $PbCl_2$ can be mixed with PbI_2 in DMF or dimethyl sulfoxide (DMSO) [49–52], and/or the second step MACl can be added [53–55]. For vapor based deposition methods, the $MAPbI_{3-x}Cl_x$ can be formed by co-evaporating MAI and $PbCl_2$ onto the substrates [56,57] or by reacting $PbCl_2$ on substrates with MAI vapor [58,59].

3. The Crystal Structure Form and Formation

3.1. Crystal Structure of $MAPbI_3$ Layer

The parameters and transitions of phases of bulk $MAPbI_3$ were included in references [60,61]. Here, we focus on the tetragonal and cubic phases [62]. In fact, there are no critical differences between the two phases, except a slight rotation of PbI_6 octahedra along the c-axis. The atomic structures of $MAPbI_3$ of the two phases are shown in Figure 1A,B. Thus, the tetragonal phase can be treated as a pseudocubic phase with $a^* = a/\sqrt{2}$, $c^* = c/2$ [63]. Below 54 °C, the cubic phase of $MAPbI_3$ can be transformed into the tetragonal phase [60], and the opposite transition occurs by annealing at 100 °C for 15 min [41]. In Figure 1C, the X-ray diffraction (XRD) patterns of the two phases are shown. After transformation to the tetragonal phase, the (100) and (200) peaks of cubic $MAPbI_3$ split, also new (211) and (213) peaks show up. Here, we use the peak splitting as indictor for phase transformation. Analysis of the $MAPbI_{3-x}Cl_x$ usually shows the cubic phase of $MAPbI_3$, however, with a much more preference along (100) and (200). This will be discussed in the Sections 3.2 and 3.3.

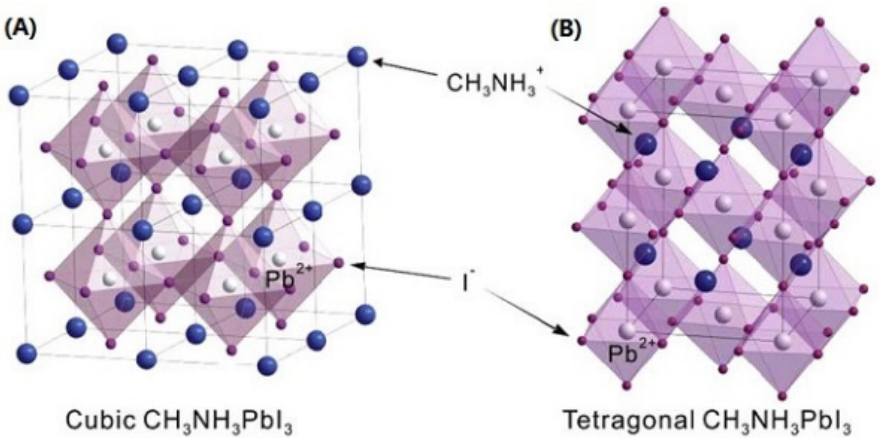

Figure 1. *Cont.*

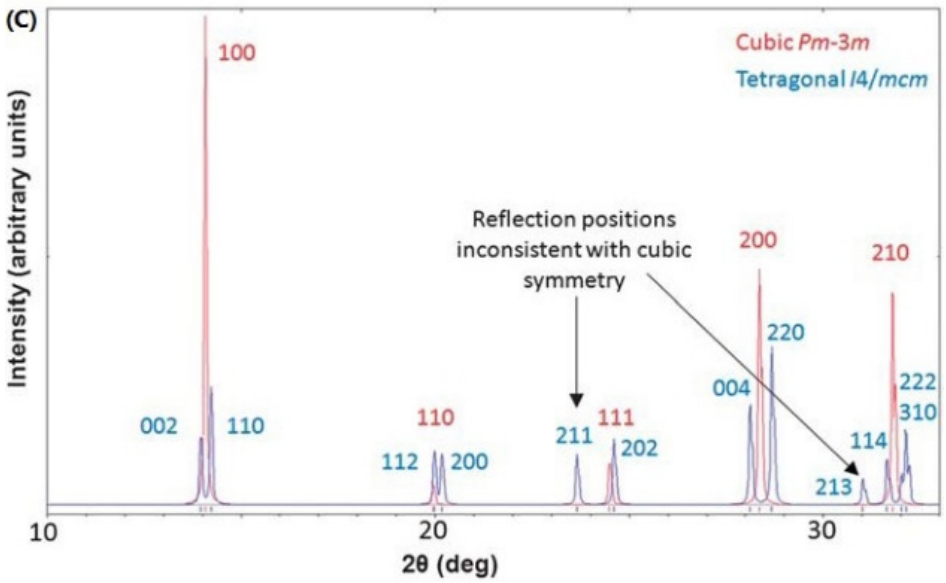

Figure 1. (**A**) Atomic models of $MAPbI_3$ with cubic phase; and (**B**) tetragonal phase; (**C**) the calculated XRD patterns for $MAPbI_3$ in both phases. (**A**) and (**B**) are reprinted from reference [64], Copyright © IOP Publishing. Reproduced with permission. All rights reserved; (**C**) is reprinted from reference [65], Copyright © 2013, Royal Society of Chemistry.

Another phase which should be noted is the amorphous phase. Pair distribution function analysis of X-ray scattering showed that after annealing at 100 °C for 30 min, the $MAPbI_3$ in meso-porous TiO_2 has about 30 atom% in medium range crystalline order and the other 70 atom% in a disordered state with a coherence length of 1.4 nm [66]. The poor crystallization of the $MAPbI_3$ in meso-porous TiO_2 was studied by high-resolution TEM [67]. Quartz crystal microbalance measurements suggest that during the sequential method only half of PbI_2 is converted to $MAPbI_3$ instantly, while the other half is involved in reversible transformation with $MAPbI_3$. Additionally, the amorphous character with a very small average crystallite size may be present after the transformation as previously discussed [68]. The amorphous phase may also present during the initially deposited $MAPbI_{3-x}Cl_x$, as indicated by the envelope in some XRD spectra. In reference [69], the amorphous phase $MA_5PbCl_4I_3$ was also mentioned. Moreover, both XRD and photoluminescence studies of $MAPbI_2Cl$ ($2MAPbI_3$+$MAPbCl_3$) indicate the existence of the amorphous phase [70].

3.2. Converting Lead Halides to Perovskite

In the sequential deposition method, PbI_2 or/and $PbCl_2$ were first dissolved in a solvent. As PbI_2 crystal has a layered structure, DMF can intercalate into the PbI_2 interlayer space and screen PbI_2 via Pb-O bonding [71–73]. When DMF is intercalated, the XRD peak of the PbI_2 (001) plane red shifts from 14.8° to 7.94° [72,73]. The red-shift of this XRD peak to 9.17° also indicates the intercalation of DMSO [43]. While $PbCl_2$ doesn't possess a similar layered structure as PbI_2, its solubility is poor where $PbCl_2$ nanoparticles may only suspend in the solvent [28]. However, depositing a mixture of PbI_2 and $PbCl_2$ on the substrates result in a new PbICl phase [74], whose crystal structure is similar to $PbCl_2$ [75].

At the beginning of the reaction of PbI_2 and MAI, a predominant peak at (220) appeared (as shown in Figure 2B). In other words, the $MAPbI_3$ preferentially grows along (220) plane at first. The annealing process increases the long range crystalline order and results in the predominant (110) peak instead. Noting the (220) is only a short range of (110), thus, another possible reason for the (110)-oriented growth of $MAPbI_{3-x}Cl_x$ and $MAPbI_3$ may be because layered crystal structure of PbI_2 (growth along (001) planes of PbI_2 like the liquid catalyst cluster model mentioned in reference [76]). The lattice planes of tetragonal $MAPbI_3$ are showed in Figure 3.

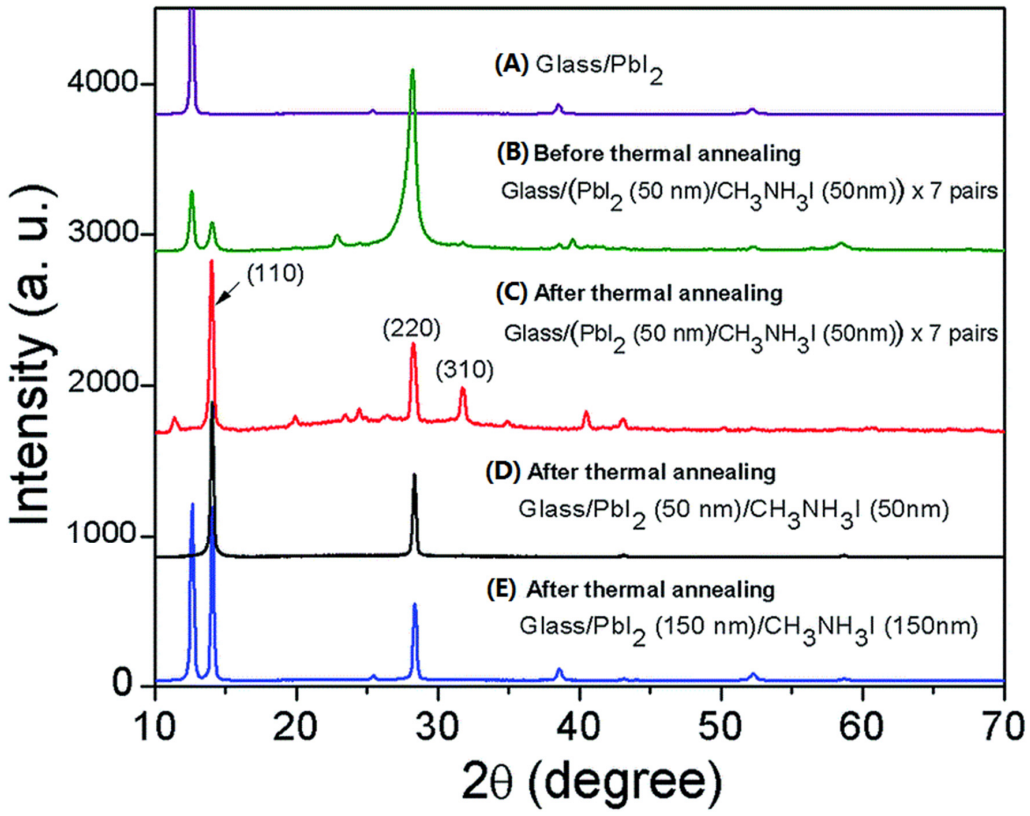

Figure 2. XRD patterns of glass substrates with vapor deposition of (**A**) a layer of PbI_2; and (**B**) a layer of PbI_2 followed by a layer of MAI, repeating this step 7 times; XRD pattern of the (**C**) annealed 7-time deposited PbI_2/MAI layer; (**D**) 1-time deposited PbI_2 (50 nm thickness)/MAI (50 nm thickness) layer; and (**E**) 1-time deposited PbI_2 (150 nm thickness)/MAI (150 nm thickness) layer. Reprinted from reference [77], Copyright © 2015, Royal Society of Chemistry.

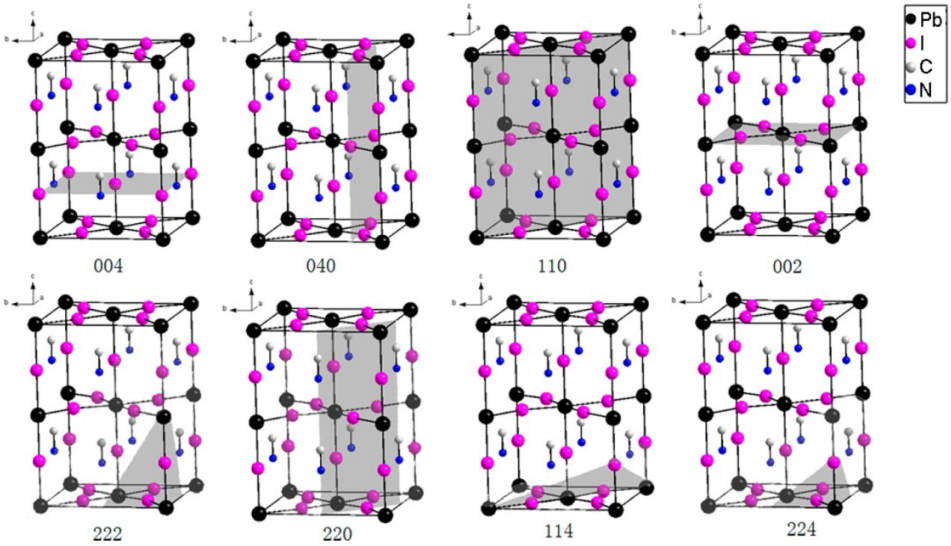

Figure 3. Crystallographic (lattice) planes (in gray) of tetragonal MAPbI3. Reprinted from reference [78], Copyright © 2015, American Chemical Society.

For $PbCl_2$, Cl^- was detached from $PbCl_2$ when the $PbCl_2$ was evaporated on the MAI substrate [79] and all the atoms of lead halide were dissociated during the crystal formation of the perovskite [80]. Thus, except the speed and the way of breaking the lead halide, the following

steps should be similar with the one step method (Section 3.3) for converting PbI_2 or $PbCl_2$ with MAI to the perovskite. However, the situation in the presence of MACl may be different. As less energy is needed for MACl than MAI to undergo phase transition from solid to gas [69], it may be easier for MACl than MAI to diffuse into the PbI_2 and cause the crystallization of perovskite [81]. However, as Cl^- cannot be incorporated into $MAPbI_3$ crystal structure, the MAI and MACl may compete with each other to determine the result crystal, because only $MAPbI_3$ or $MAPbCl_3$ was formed when PbI2 was soaked in 80 mM MAI + 40 mM MACl or in 40 mM MAI + 80 mM MACl, respectively [80]. Thus, the incorporation of some amount of MACl managed to modify the morphology of the perovskite and resulted in better performance of the solar cells.

3.3. One Step Deposition of $MAPbI_{3-x}Cl_x$

The better crystallization of $MAPbI_{3-x}Cl_x$ along (110) and (220) plane of the tetragonal phase or (100) and (200) planes of the cubic phase may be due to the lowered cubic-tetragonal phase transition temperature of $MAPbI_{3-x}Cl_x$ after the incorporation of Cl^- [82]. A clear cubic-tetragonal phase transition temperature of $MAPbI_3$ was detected by differential scanning calorimeter (DSC) analysis [65], however no such phase transition was observed for $MAPbI_{3-x}Cl_x$ [83]. To explain the absence of the phase transition for $MAPbI_{3-x}Cl_x$, we first study the crystallization process of $MAPbI_{3-x}Cl_x$ by one step deposition method.

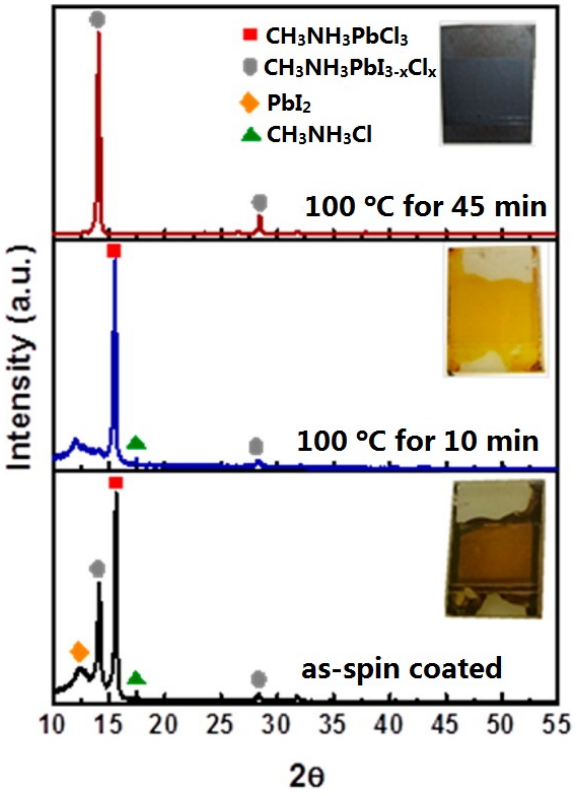

Figure 4. XRD patterns and optical images (insets) of $MAPbI_{3-x}Cl_x$ film during annealing. Reprinted from reference [84], Copyright © 2015, American Chemical Society.

Detail information about crystal formation process of $MAPbI_3$ is summarized in reference [85]. For $MAPbI_{3-x}Cl_x$, the transformation from the intermediate phase to the perovskite is determined as 80 °C by *in situ* grazing incidence wide-angle X-ray scattering (GIWAXS) [86]. Figure 4 presents a clearer picture of the crystal formation of $MAPbI_{3-x}Cl_x$. The 15.7° and 31.5° peaks are associated with the (100) and (200) diffraction peaks of $MAPbCl_3$ [82]. These peaks were also observed in references [27,87,88]. In Figure 4, it is interesting to note that MAPbI3 was formed first for the as-spin coated film but

converted to $MAPbCl_3$ after annealing at 100 °C for 10 min, and then $MAPbCl_3$ was converted back to $MAPbI_3$ after 45 min of annealing [84]. Further annealing would result in the decomposition of $MAPbI_3$ to PbI_2, but this occurred after conversion to the intermediate phase to $MAPbI_3$ [89]. Because $MAPbCl_3$ is in a cubic phase, we suppose that $MAPbCl_3$ may cause a template effect for the cubic $MAPbI_3$ phase.

In addition, the MAI:PbI_2 (molar ratio 3:1) precursor solution on compact TiO_2 can also form $MAPbI_3$ with a predominant (110) plane, but the annealing temperature need to be above 150 °C [84,88,90]. The different sublimation temperature of MAI and MACl and the evidence of residue MAI or MACl in the resulting perovskite may explain the higher annealing temperature needed for $MAPbI_3$ [84,91].

The XRD patterns of the resulting $MAPbI_{3-x}Cl_x$ prepared from different chloride-containing precursors are summarized in Figure 5. All the patterns showed predominant crystallization along the (110) and (220) planes. Interestingly, the (220) peak split at a high MACl (x = 2) concentration in Figure 5B [27]. This split was also observed in reference [29]. In the sequential deposition method, the (110) and (220) crystallization preference may be due to an *in situ* transformation process [92] of PbI_2 to $MAPbI_3$, as discussed in Section 3.2. However, the PbI_6 octahedra are more likely to be fully dissociated in the one step precursor solution. [29,93–95] As MACl does not fit in the $MAPbI_3$ structure, it could be possible that MACl may be expelled along the (110) planes of the $MAPbI_3$ and that is why the $MAPbI_{3-x}Cl_x$ always showed the (110) and (220) orientation preference. This assumption can be proved by (220) peak split in Figure 5B, as excess of MACl breaks down the crystal range along (110) planes resulting in peak split. However, MAI can fit in the $MAPbI_3$ structure, (110)-oriented growth is just the result of cubic phase in high temperature (150 °C in refereneces [84,88,90]). Surprisingly, a main XRD peak of (310) was observed for the one step deposition prepared $MAPbI_3$ [96]. The main peak of (310), which is distinct from the (110) peak, may have resulted from the fact that the MAI was added into the precursor solution after the PbI_2 was completely dissolved instead of both MAI and PbI_2 being present at the same time [96], or the fact that the (310) plane of $MAPbI_3$ may match the crystal structure of the substrate better. Then the magnitude of the (110) peak of $MAPbI_{3-x}Cl_x$ and the (310) peak of $MAPbI_3$ further increases after 5 weeks [96]. Thus, we believe that the annealing process may only reinforce the crystallization preference as it is initially formed and the effects of substrate also contribute to the crystal structure formation of the perovskite in some cases. Returning to Figure 5, if excess of MACl breaks down the growth along the (110) plane, we believe MACl can also break down the crystalline order range. Since a large amount of $MAPbI_3$ existed in the amorphous phase form, the cubic phase of $MAPbI_3$ may be more favorable in short crystalline order range than the tetragonal phase.

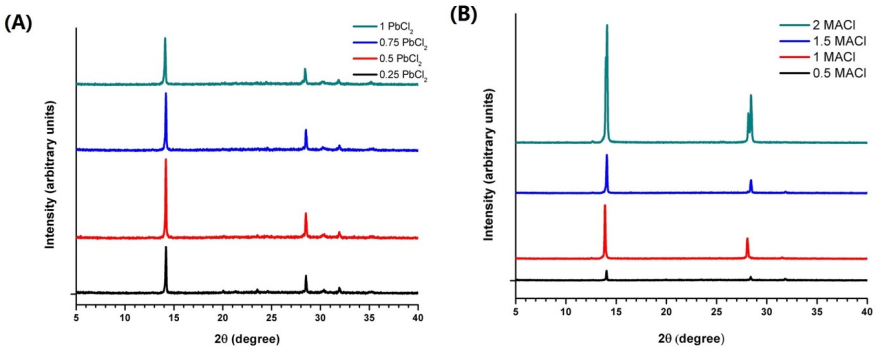

Figure 5. XRD patterns of $MAPbI_{3-x}Cl_x$ prepared from (**A**) precursor solution $xPbCl_2+yPbI_2+zMAI$ (x = 0.25, 0.5, 0.75 and 1; y = 1 − x; z = 3 × x + y) in DMF; and (**B**) precursor solution $1PbI_2+1MAI+xMACl$ (x = 0.5, 1, 1.5 and 2). Reprinted from reference [27], Copyright © 2014, American Chemical Society.

There are other influences associated with Cl^-. Increasing the temperature during the soaking of the PbI_2 substrate in MAI + MACl IPA solution can improve the (110) orientation of $MAPbI_{3-x}Cl_x$ where the high temperature facilitates the expelling of MACl [97]. Annealing the MACl:PbI_2 (3:1) precursor on compact TiO_2 at 60 °C for 10 min followed by 100 °C for 20 min instead of gradually heating from 25 to 100 °C for 45 min resulted in the (200) crystal plane of $MAPbI_{3-x}Cl_x$ being vertically aligned on the substrate [98]. The tetragonal phase $MAPbI_{3-x}Cl_x$ was occasionally found on compact TiO_2 substrate [53], while the cubic phase always occurred in meso-porous substrate, where the trapped MACl in meso-porous structure [8] helps the formation of cubic phase. While the size of $MAPbI_3$ crystal grains are smaller but the degree of crystallinity improves in the presence of MACl [27,54], the sequential deposited $MAPbI_{3-x}Cl_x$ results in (001) elongated crystals [13].

4. Conclusions

In this article, the location of Cl^- and its influence on the crystal morphology of $MAPbI_{3-x}Cl_x$ is summarized, where the deposition methods (one step deposition, sequential deposition and vapor based deposition) for $MAPbI_{3-x}Cl_x$ are reviewed. Furthermore, the cubic and tetragonal phases of $MAPbI_3$ are elucidated and the crystallization process of $MAPbI_{3-x}Cl_x$ is also summarized. Detailed information about the crystal structure with variable deposition parameters is also discussed. Though a recent report showed that Cl^- mainly improves the carrier transport at the perovskite/Spiro-MeOTAD and perovskite/TiO_2 interfaces, rather than within the perovskite crystals, the authors of reference [99] more recently spatially resolved photoluminescence decay results showed less recombination in the high chlorine concentration region [100]. Thus, the effect of high concentration of Cl^- on the morphologies and electronic properties of the perovskite can still not be ignored. Additionally, whether Cl^- is predominantly present as a substituent for I^-, as an interstitial, or at the surface of the crystal, remains unclear [101] and this is worth further investigation.

Conflicts of Interest: The authors declare no conflict of interest.

References

1. Kojima, A.; Teshima, K.; Shirai, Y.; Miyasaka, T. Organometal halide perovskites as visible-light sensitizers for photovoltaic cells. *J. Am. Chem Soc.* **2009**, *131*, 6050–6051. [CrossRef] [PubMed]
2. Yang, W.S.; Noh, J.H.; Jeon, N.J.; Kim, Y.C.; Ryu, S.; Seo, J.; Seok, S.I. High-performance photovoltaic perovskite layers fabricated through intramolecular exchange. *Science* **2015**, *348*, 1234–1237. [CrossRef] [PubMed]
3. Kim, H.S.; Im, S.H.; Park, N.G. Organolead halide perovskite: New horizons in solar cell research. *J. Phys. Chem. C* **2014**, *118*, 5615–5625. [CrossRef]
4. Luo, S.; Daoud, W.A. Recent progress in organic-inorganic halide perovskite solar cells: Mechanisms and materials design. *J. Mater. Chem. A* **2015**, *3*, 8992–9010. [CrossRef]
5. Mohammad, K.N.; Gao, P.; Gratzel, M. Organohalide lead perovskites for photovoltaic applications. *Energ. Environ. Sci.* **2014**, *7*, 2448–2463.
6. Dualeh, A.; Tétreault, N.; Moehl, T.; Gao, P.; Nazeeruddin, M.K.; Grätzel, M. Effect of annealing temperature on film morphology of organic-inorganic hybrid pervoskite solid-state solar cells. *Adv. Funct. Mater.* **2014**, *24*, 3250–3258. [CrossRef]
7. Stranks, S.D.; Eperon, G.E.; Grancini, G.; Menelaou, C.; Alcocer, M.J.P.; Leijtens, T.; Herz, L.M.; Petrozza, A.; Snaith, H.J. Electron-hole diffusion lengths exceeding 1 micrometer in an organometal trihalide perovskite absorber. *Science* **2013**, *342*, 341–344. [CrossRef] [PubMed]
8. Colella, S.; Mosconi, E.; Fedeli, P.; Listorti, A.; Gazza, F.; Orlandi, F.; Ferro, P.; Besagni, T.; Rizzo, A.; Calestani, G.; *et al*. $MAPbI_{3-x}Cl_x$ mixed halide perovskite for hybrid solar cells: The role of chloride as dopant on the transport and structural properties. *Chem Mater.* **2013**, *25*, 4613–4618. [CrossRef]
9. Conings, B.; Baeten, L.; de Dobbelaere, C.; D'Haen, J.; Manca, J.; Boyen, H.-G. Perovskite-based hybrid solar cells exceeding 10% efficiency with high reproducibility using a thin film sandwich approach. *Adv. Mater.* **2014**, *26*, 2041–2046. [CrossRef] [PubMed]

10. Zhao, Y.; Zhu, K. CH_3NH_3Cl-assisted one-step solution growth of $CH_3NH_3PbI_3$: Structure, charge-carrier dynamics, and photovoltaic properties of perovskite solar cells. *J. Phys. Chem. C* **2014**, *118*, 9412–9418. [CrossRef]
11. Colella, S.; Mosconi, E.; Pellegrino, G.; Alberti, A.; Guerra, V.L.P.; Masi, S.; Listorti, A.; Rizzo, A.; Condorelli, G.G.; De Angelis, F.; *et al*. Elusive presence of chloride in mixed halide perovskite solar cells. *J. Phys. Chem. Lett.* **2014**, *5*, 3532–3538. [CrossRef] [PubMed]
12. Unger, E.L.; Bowring, A.R.; Tassone, C.J.; Pool, V.L.; Gold-Parker, A.; Cheacharoen, R.; Stone, K.H.; Hoke, E.T.; Toney, M.F.; McGehee, M.D. Chloride in lead chloride-derived organo-metal halides for perovskite-absorber solar cells. *Chem. Mater.* **2014**, *26*, 7158–7165. [CrossRef]
13. Dar, M.I.; Arora, N.; Gao, P.; Ahmad, S.; Grätzel, M.; Nazeeruddin, M.K. Investigation regarding the role of chloride in organic-inorganic halide perovskites obtained from chloride containing precursors. *Nano Lett.* **2014**, *14*, 6991–6996. [CrossRef] [PubMed]
14. Tripathi, N.; Yanagida, M.; Shirai, Y.; Masuda, T.; Han, L.; Miyano, K. Hysteresis-free and highly stable perovskite solar cells produced via a chlorine-mediated interdiffusion method. *J. Mater. Chem. A* **2015**, *3*, 12081–12088. [CrossRef]
15. Starr, D.E.; Sadoughi, G.; Handick, E.; Wilks, R.G.; Alsmeier, J.H.; Kohler, L.; Gorgoi, M.; Snaith, H.J.; Bar, M. Direct observation of an inhomogeneous chlorine distribution in $CH_3NH_3PbI_{3-x}Cl_x$ layers: Surface depletion and interface enrichment. *Energ. Environ. Sci.* **2015**, *8*, 1609–1615. [CrossRef]
16. Pool, V.L.; Gold-Parker, A.; McGehee, M.D.; Toney, M.F. Chlorine in $PbCl_2$-derived hybrid-perovskite solar absorbers. *Chem. Mater.* **2015**, *27*, 7240–7243. [CrossRef]
17. Chae, J.; Dong, Q.; Huang, J.; Centrone, A. Chloride incorporation process in $CH_3NH_3PbI_{3-x}Cl_x$ perovskites via nanoscale bandgap maps. *Nano Lett.* **2015**, *15*, 8114–8121. [CrossRef] [PubMed]
18. Mosconi, E.; Amat, A.; Nazeeruddin, M.K.; Grätzel, M.; De Angelis, F. First-principles modeling of mixed halide organometal perovskites for photovoltaic applications. *J. Phys. Chem. C* **2013**, *117*, 13902–13913. [CrossRef]
19. Zheng, F.; Takenaka, H.; Wang, F.; Koocher, N.Z.; Rappe, A.M. First-principles calculation of the bulk photovoltaic effect in $CH_3NH_3PbI_3$ and $CH_3NH_3PbI_{3-x}Cl_x$. *J. Phys. Chem. Lett.* **2014**, *6*, 31–37. [CrossRef] [PubMed]
20. Buin, A.; Pietsch, P.; Xu, J.; Voznyy, O.; Ip, A.H.; Comin, R.; Sargent, E.H. Materials processing routes to trap-free halide perovskites. *Nano Lett.* **2014**, *14*, 6281–6286. [CrossRef] [PubMed]
21. Du, M.H. Efficient carrier transport in halide perovskites: Theoretical perspectives. *J. Mater. Chem. A* **2014**, *2*, 9091–9098. [CrossRef]
22. Even, J.; Pedesseau, L.; Katan, C. Analysis of multivalley and multibandgap absorption and enhancement of free carriers related to exciton screening in hybrid perovskites. *J. Phys. Chem. C* **2014**, *118*, 11566–11572. [CrossRef]
23. Yin, W.-J.; Shi, T.; Yan, Y. Unique properties of halide perovskites as possible origins of the superior solar cell performance. *Adv. Mater.* **2014**, *26*, 4653–4658. [CrossRef] [PubMed]
24. Li, D.; Liang, C.; Zhang, H.; Zhang, C.; You, F.; He, Z. Spatially separated charge densities of electrons and holes in organic-inorganic halide perovskites. *J. Appl. Phys.* **2015**, *117*, 074901. [CrossRef]
25. Yin, J.; Cortecchia, D.; Krishna, A.; Chen, S.; Mathews, N.; Grimsdale, A.C.; Soci, C. Interfacial charge transfer anisotropy in polycrystalline lead iodide perovskite films. *J. Phys. Chem. Lett.* **2015**, 1396–1402. [CrossRef] [PubMed]
26. Mosconi, E.; Ronca, E.; De Angelis, F. First-principles investigation of the Tio_2/organohalide perovskites interface: The role of interfacial chlorine. *J. Phys. Chem. Lett.* **2014**, *5*, 2619–2625. [CrossRef] [PubMed]
27. Williams, S.T.; Zuo, F.; Chueh, C.-C.; Liao, C.-Y.; Liang, P.-W.; Jen, A.K.Y. Role of chloride in the morphological evolution of organo-lead halide perovskite thin films. *Acs Nano* **2014**, *8*, 10640–10654. [CrossRef] [PubMed]
28. Tidhar, Y.; Edri, E.; Weissman, H.; Zohar, D.; Hodes, G.; Cahen, D.; Rybtchinski, B.; Kirmayer, S. Crystallization of methyl ammonium lead halide perovskites: Implications for photovoltaic applications. *J. Am. Chem. Soc.* **2014**, *136*, 13249–13256. [CrossRef] [PubMed]
29. Yan, K.; Long, M.; Zhang, T.; Wei, Z.; Chen, H.; Yang, S.; Xu, J. Hybrid halide perovskite solar cell precursors: Colloidal chemistry and coordination engineering behind device processing for high efficiency. *J. Am. Chem. Soc.* **2015**, *137*, 4460–4468. [CrossRef]

30. Zheng, L.; Zhang, D.; Ma, Y.; Lu, Z.; Chen, Z.; Wang, S.; Xiao, L.; Gong, Q. Morphology control of the perovskite films for efficient solar cells. *Dalton Trans.* **2015**, *44*, 10582–10593. [CrossRef] [PubMed]
31. Kim, H.S.; Lee, C.R.; Im, J.H.; Lee, K.B.; Moehl, T.; Marchioro, A.; Moon, S.J.; Humphry-Baker, R.; Yum, J.H.; Moser, J.E.; *et al*. Lead iodide perovskite sensitized all-solid-state submicron thin film mesoscopic solar cell with efficiency exceeding 9%. *Sci. Rep.* **2012**, *2*. [CrossRef]
32. Lee, M.M.; Teuscher, J.; Miyasaka, T.; Murakami, T.N.; Snaith, H.J. Efficient hybrid solar cells based on meso-superstructured organometal halide perovskites. *Science* **2012**, *338*, 643–647. [CrossRef] [PubMed]
33. Saliba, M.; Tan, K.W.; Sai, H.; Moore, D.T.; Scott, T.; Zhang, W.; Estroff, L.A.; Wiesner, U.; Snaith, H.J. Influence of thermal processing protocol upon the crystallization and photovoltaic performance of organic-inorganic lead trihalide perovskites. *J. Phys. Chem. C* **2014**, *118*, 17171–17177. [CrossRef]
34. Hsu, H.-L.; Chen, C.; Chang, J.-Y.; Yu, Y.-Y.; Shen, Y.-K. Two-step thermal annealing improves the morphology of spin-coated films for highly efficient perovskite hybrid photovoltaics. *Nanoscale* **2014**, *6*, 10281–10288. [CrossRef] [PubMed]
35. Kang, R.; Kim, J.-E.; Yeo, J.-S.; Lee, S.; Jeon, Y.-J.; Kim, D.-Y. Optimized organometal halide perovskite planar hybrid solar cells via control of solvent evaporation rate. *J. Phys. Chem. C* **2014**, *118*, 26513–26520. [CrossRef]
36. Guo, Y.; Liu, C.; Inoue, K.; Harano, K.; Tanaka, H.; Nakamura, E. Enhancement in the efficiency of an organic-inorganic hybrid solar cell with a doped P3HT hole-transporting layer on a void-free perovskite active layer. *J. Mater. Chem. A* **2014**, *2*, 13827–13830. [CrossRef]
37. Liang, P.-W.; Liao, C.-Y.; Chueh, C.-C.; Zuo, F.; Williams, S.T.; Xin, X.-K.; Lin, J.; Jen, A.K.Y. Additive enhanced crystallization of solution-processed perovskite for highly efficient planar-heterojunction solar cells. *Adv. Mater.* **2014**, *26*, 3748–3754. [CrossRef] [PubMed]
38. Chueh, C.-C.; Liao, C.-Y.; Zuo, F.; Williams, S.T.; Liang, P.-W.; Jen, A.K.Y. The roles of alkyl halide additives in enhancing perovskite solar cell performance. *J. Mater. Chem. A* **2014**, *3*, 9058–9062. [CrossRef]
39. Ding, Y.; Yao, X.; Zhang, X.; Wei, C.; Zhao, Y. Surfactant enhanced surface coverage of $CH_3NH_3PbI_{3-x}Cl_x$ perovskite for highly efficient mesoscopic solar cells. *J. Power Sources* **2014**, *272*, 351–355. [CrossRef]
40. Eperon, G.E.; Burlakov, V.M.; Docampo, P.; Goriely, A.; Snaith, H.J. Morphological control for high performance, solution-processed planar heterojunction perovskite solar cells. *Adv. Funct. Mater.* **2014**, *24*, 151–157. [CrossRef]
41. Takeo, O.; Masahito, Z.; Yuma, I.; Atsushi, S.; Kohei, S. Microstructures and photovoltaic properties of perovskite-type $CH_3NH_3PbI_3$ compounds. *Appl. Phys. Express.* **2014**, *7*. [CrossRef]
42. Jeon, Y.-J.; Lee, S.; Kang, R.; Kim, J.-E.; Yeo, J.-S.; Lee, S.-H.; Kim, S.-S.; Yun, J.-M.; Kim, D.-Y. Planar heterojunction perovskite solar cells with superior reproducibility. *Sci. Rep.* **2014**, *4*. [CrossRef] [PubMed]
43. Jeon, N.J.; Noh, J.H.; Kim, Y.C.; Yang, W.S.; Ryu, S.; Seok, S.I. Solvent engineering for high-performance inorganic-organic hybrid perovskite solar cells. *Nat. Mater.* **2014**, *13*, 897–903. [CrossRef] [PubMed]
44. Xiao, M.; Huang, F.; Huang, W.; Dkhissi, Y.; Zhu, Y.; Etheridge, J.; Gray-Weale, A.; Bach, U.; Cheng, Y.-B.; Spiccia, L. A fast deposition-crystallization procedure for highly efficient lead iodide perovskite thin-film solar cells. *Angew. Chem.* **2014**, *126*, 10056–10061. [CrossRef]
45. Jung, J.W.; Williams, S.T.; Jen, A.K.Y. Low-temperature processed high-performance flexible perovskite solar cells via rationally optimized solvent washing treatments. *Rsc Adv.* **2014**, *4*, 62971–62977. [CrossRef]
46. Ito, S.; Tanaka, S.; Vahlman, H.; Nishino, H.; Manabe, K.; Lund, P. Carbon-double-bond-free printed solar cells from $TiO_2/CH_3NH_3PbI_3/CuSCN/Au$: Structural control and photoaging effects. *Chem. Phys. Chem.* **2014**, *15*, 1194–1200. [CrossRef] [PubMed]
47. Huang, F.; Dkhissi, Y.; Huang, W.; Xiao, M.; Benesperi, I.; Rubanov, S.; Zhu, Y.; Lin, X.; Jiang, L.; Zhou, Y.; *et al*. Gas-assisted preparation of lead iodide perovskite films consisting of a monolayer of single crystalline grains for high efficiency planar solar cells. *Nano Energy* **2014**, *10*, 10–18. [CrossRef]
48. Burschka, J.; Pellet, N.; Moon, S.J.; Humphry-Baker, R.; Gao, P.; Nazeeruddin, M.K.; Gratzel, M. Sequential deposition as a route to high-performance perovskite-sensitized solar cells. *Nature* **2013**, *499*, 316–320. [CrossRef] [PubMed]
49. Ma, Y.; Zheng, L.; Chung, Y.-H.; Chu, S.; Xiao, L.; Chen, Z.; Wang, S.; Qu, B.; Gong, Q.; Wu, Z.; *et al*. A highly efficient mesoscopic solar cell based on $CH_3NH_3PbI_{3-x}Cl_x$ fabricated via sequential solution deposition. *Chem. Commun.* **2014**, *50*, 12458–12461. [CrossRef] [PubMed]

50. Zheng, L.; Ma, Y.; Chu, S.; Wang, S.; Qu, B.; Xiao, L.; Chen, Z.; Gong, Q.; Wu, Z.; Hou, X. Improved light absorption and charge transport for perovskite solar cells with rough interfaces by sequential deposition. *Nanoscale* **2014**, *6*, 8171–8176. [CrossRef] [PubMed]
51. Dar, M.I.; Abdi-Jalebi, M.; Arora, N.; Grätzel, M.; Nazeeruddin, M.K. Growth engineering of $CH_3NH_3PbI_3$ structures for high-efficiency solar cells. *Adv. Energy Mater.* **2016**, *6*. [CrossRef]
52. Li, Y.; Sun, W.; Yan, W.; Ye, S.; Peng, H.; Liu, Z.; Bian, Z.; Huang, C. High-performance planar solar cells based on $CH_3NH_3PbI_{3-x}Cl_x$ perovskites with determined chlorine mole fraction. *Adv. Funct. Mater.* **2015**, *25*, 4867–4873. [CrossRef]
53. Docampo, P.; Hanusch, F.; Stranks, S.D.; Döblinger, M.; Feckl, J.M.; Ehrensperger, M.; Minar, N.K.; Johnston, M.B.; Snaith, H.J.; Bein, T. Solution deposition-conversion for planar heterojunction mixed halide perovskite solar cells. *Adv. Energy Mater.* **2014**, *4*. [CrossRef]
54. Jiang, M.; Wu, J.; Lan, F.; Tao, Q.; Gao, D.; Li, G. Enhancing the performance of planar organo-lead halide perovskite solar cells by using mixed halide source. *J. Mater. Chem. A* **2014**, *3*, 963–967. [CrossRef]
55. Dong, Q.; Yuan, Y.; Shao, Y.; Fang, Y.; Wang, Q.; Huang, J. Abnormal crystal growth in $CH_3NH_3PbI_{3-x}Cl_x$ using a multi-cycle solution coating process. *Energ. Environ. Sci.* **2015**, *8*, 2464–2470. [CrossRef]
56. Liu, M.; Johnston, M.B.; Snaith, H.J. Efficient planar heterojunction perovskite solar cells by vapour deposition. *Nature* **2013**, *501*, 395–398. [CrossRef] [PubMed]
57. Ono, L.K.; Wang, S.; Kato, Y.; Raga, S.R.; Qi, Y. Fabrication of semi-transparent perovskite films with centimeter-scale superior uniformity by the hybrid deposition method. *Energ. Environ. Sci.* **2014**, *7*, 3989–3993. [CrossRef]
58. Leyden, M.R.; Ono, L.K.; Raga, S.R.; Kato, Y.; Wang, S.; Qi, Y. High performance perovskite solar cells by hybrid chemical vapor deposition. *J. Mater. Chem. A* **2014**, *2*, 18742–18745. [CrossRef]
59. Chen, C.-W.; Kang, H.-W.; Hsiao, S.-Y.; Yang, P.-F.; Chiang, K.-M.; Lin, H.-W. Efficient and uniform planar-type perovskite solar cells by simple sequential vacuum deposition. *Adv. Mater.* **2014**, *26*, 6647–6652. [CrossRef] [PubMed]
60. Poglitsch, A.; Weber, D. Dynamic disorder in methylammoniumtrihalogenoplumbates (ii) observed by millimeter-wave spectroscopy. *J. Chem. Phys.* **1987**, *87*, 6373–6378. [CrossRef]
61. Stoumpos, C.C.; Malliakas, C.D.; Kanatzidis, M.G. Semiconducting tin and lead iodide perovskites with organic cations: Phase transitions, high mobilities, and near-infrared photoluminescent properties. *Inorg. Chem.* **2013**, *52*, 9019–9038. [CrossRef] [PubMed]
62. Kawamura, Y.; Mashiyama, H.; Hasebe, K. Structural study on cubic–tetragonal transition of $CH_3NH_3PbI_3$. *J. Phy. Soc. Jpn.* **2002**, *71*, 1694–1697. [CrossRef]
63. Eperon, G.E.; Stranks, S.D.; Menelaou, C.; Johnston, M.B.; Herz, L.M.; Snaith, H.J. Formamidinium lead trihalide: A broadly tunable perovskite for efficient planar heterojunction solar cells. *Energ. Environ. Sci.* **2014**, *7*, 982–988. [CrossRef]
64. Chen, Z.; Li, H.; Tang, Y.; Huang, X.; Ho, D.; Lee, C.-S. Shape-controlled synthesis of organolead halide perovskite nanocrystals and their tunable optical absorption. *Mater. Res. Express* **2014**, *1*. [CrossRef]
65. Baikie, T.; Fang, Y.N.; Kadro, J.M.; Schreyer, M.; Wei, F.X.; Mhaisalkar, S.G.; Graetzel, M.; White, T.J. Synthesis and crystal chemistry of the hybrid perovskite $CH_3NH_3PbI_3$ for solid-state sensitised solar cell applications. *J. Mater. Chem. A* **2013**, *1*, 5628–5641. [CrossRef]
66. Choi, J.J.; Yang, X.H.; Norman, Z.M.; Billinge, S.J.L.; Owen, J.S. Structure of methylammonium lead iodide within mesoporous titanium dioxide: Active material in high-performance perovskite solar cells. *Nano Lett.* **2014**, *14*, 127–133. [CrossRef] [PubMed]
67. Zhou, Y.; Vasiliev, A.L.; Wu, W.; Yang, M.; Pang, S.; Zhu, K.; Padture, N.P. Crystal morphologies of organolead trihalide in mesoscopic/planar perovskite solar cells. *J. Phys. Chem. Lett.* **2015**, *6*, 2292–2297. [CrossRef] [PubMed]
68. Harms, H.A.; Tetreault, N.; Pellet, N.; Bensimon, M.; Gratzel, M. Mesoscopic photosystems for solar light harvesting and conversion: Facile and reversible transformation of metal-halide perovskites. *Faraday Discuss.* **2014**, *176*, 251–269. [CrossRef] [PubMed]
69. Dualeh, A.; Gao, P.; Seok, S.I.; Nazeeruddin, M.K.; Grätzel, M. Thermal behavior of methylammonium lead-trihalide perovskite photovoltaic light harvesters. *Chem Mater.* **2014**, *26*, 6160–6164. [CrossRef]

70. Park, B.-W.; Jain, S.M.; Zhang, X.; Hagfeldt, A.; Boschloo, G.; Edvinsson, T. Resonance raman and excitation energy dependent charge transfer mechanism in halide-substituted hybrid perovskite solar cells. *Acs Nano* **2015**, *9*, 2088–2101. [CrossRef] [PubMed]
71. Wakamiya, A.; Endo, M.; Sasamori, T.; Tokitoh, N.; Ogomi, Y.; Hayase, S.; Murata, Y. Reproducible fabrication of efficient perovskite-based solar cells: X-ray crystallographic studies on the formation of $CH_3NH_3PbI_3$ layers. *Chem. Lett.* **2014**, *43*, 711–713. [CrossRef]
72. Hao, F.; Stoumpos, C.C.; Liu, Z.; Chang, R.P.H.; Kanatzidis, M.G. Controllable perovskite crystallization at a gas-solid interface for hole conductor-free solar cells with steady power conversion efficiency over 10%. *J. Am. Chem. Soc.* **2014**, *136*, 16411–16419. [CrossRef] [PubMed]
73. Shen, D.; Yu, X.; Cai, X.; Peng, M.; Ma, Y.; Su, X.; Xiao, L.; Zou, D. Understanding the solvent-assisted crystallization mechanism inherent in efficient organic-inorganic halide perovskite solar cells. *J. Mater. Chem. A* **2014**, *2*, 20454–20461. [CrossRef]
74. Li, Y.; Cooper, J.K.; Buonsanti, R.; Giannini, C.; Liu, Y.; Toma, F.M.; Sharp, I.D. Fabrication of planar heterojunction perovskite solar cells by controlled low-pressure vapor annealing. *J. Phys. Chem. Lett.* **2015**, *6*, 493–499. [CrossRef] [PubMed]
75. Brixner, L.H.; Chen, H.Y.; Foris, C.M. X-ray study of the $PbCl_{2-x}I_x$ and $PbBr_{2-x}I_x$ systems. *J. Solid State Chem.* **1981**, *40*, 336–343. [CrossRef]
76. Im, J.-H.; Luo, J.; Franckevičius, M.; Pellet, N.; Gao, P.; Moehl, T.; Zakeeruddin, S.M.; Nazeeruddin, M.K.; Grätzel, M.; Park, N.-G. Nanowire perovskite solar cell. *Nano Lett.* **2015**, *15*, 2120–2126. [CrossRef] [PubMed]
77. Ng, A.; Ren, Z.; Shen, Q.; Cheung, S.H.; Gokkaya, H.C.; Bai, G.; Wang, J.; Yang, L.; So, S.K.; Djurisic, A.B.; *et al*. Efficiency enhancement by defect engineering in perovskite photovoltaic cells prepared using evaporated PbI_2/CH_3NH_3I multilayers. *J. Mater. Chem. A* **2015**, *3*, 9223–9231. [CrossRef]
78. Zhu, F.; Men, L.; Guo, Y.; Zhu, Q.; Bhattacharjee, U.; Goodwin, P.M.; Petrich, J.W.; Smith, E.A.; Vela, J. Shape evolution and single particle luminescence of organometal halide perovskite nanocrystals. *Acs Nano* **2015**, *9*, 2948–2959. [CrossRef] [PubMed]
79. Ng, T.-W.; Chan, C.-Y.; Lo, M.-F.; Guan, Z.Q.; Lee, C.-S. Formation chemistry of perovskites with mixed iodide/chloride content and the implications on charge transport properties. *J. Mater. Chem. A* **2015**, *3*, 9081–9085. [CrossRef]
80. Moore, D.T.; Sai, H.; Tan, W.K.; Estroff, L.A.; Wiesner, U. Impact of the organic halide salt on final perovskite composition for photovoltaic applications. *APL Mater.* **2014**, *2*. [CrossRef]
81. Xu, Y.; Zhu, L.; Shi, J.; Lv, S.; Xu, X.; Xiao, J.; Dong, J.; Wu, H.; Luo, Y.; Li, D.; *et al*. Efficient hybrid mesoscopic solar cells with morphology-controlled $CH_3NH_3PbI_{3-x}Cl_x$ derived from two-step spin coating method. *Acs Appl. Mater. Inter.* **2015**, *7*, 2242–2248. [CrossRef] [PubMed]
82. Pistor, P.; Borchert, J.; Fränzel, W.; Csuk, R.; Scheer, R. Monitoring the phase formation of co-evaporated lead halide perovskite thin films by *in situ* XRD. *J. Phys. Chem. Lett.* **2014**, *5*, 3308–3312. [CrossRef] [PubMed]
83. Williams, A.E.; Holliman, P.J.; Carnie, M.J.; Davies, M.L.; Worsley, D.A.; Watson, T.M. Perovskite processing for photovoltaics: A spectro-thermal evaluation. *J. Mater. Chem. A* **2014**, *2*, 19338–19346. [CrossRef]
84. Yantara, N.; Yanan, F.; Shi, C.; Dewi, H.A.; Boix, P.P.; Mhaisalkar, S.G.; Mathews, N. Unravelling the effects of Cl addition in single step $CH_3NH_3PbI_3$ perovskite solar cells. *Chem. Mater.* **2015**, *27*, 2309–2314. [CrossRef]
85. Song, Z.; Watthage, S.C.; Phillips, A.B.; Tompkins, B.L.; Ellingson, R.J.; Heben, M.J. Impact of processing temperature and composition on the formation of methylammonium lead iodide perovskites. *Chem. Mater.* **2015**, *27*, 4612–4619. [CrossRef]
86. Tan, K.W.; Moore, D.T.; Saliba, M.; Sai, H.; Estroff, L.A.; Hanrath, T.; Snaith, H.J.; Wiesner, U. Thermally induced structural evolution and performance of mesoporous block copolymer-directed alumina perovskite solar cells. *Acs Nano* **2014**, *8*, 4730–4739. [CrossRef] [PubMed]
87. Zhou, H.; Chen, Q.; Li, G.; Luo, S.; Song, T.-b.; Duan, H.-S.; Hong, Z.; You, J.; Liu, Y.; Yang, Y. Interface engineering of highly efficient perovskite solar cells. *Science* **2014**, *345*, 542–546. [CrossRef] [PubMed]
88. Yu, H.; Wang, F.; Xie, F.; Li, W.; Chen, J.; Zhao, N. The role of chlorine in the formation process of "$CH_3NH_3PbI_{3-x}Cl_x$" perovskite. *Adv. Funct. Mater.* **2014**, *24*, 7102–7108. [CrossRef]
89. Song, T.-B.; Chen, Q.; Zhou, H.; Luo, S.; Yang, Y.; You, J. Unraveling film transformations and device performance of planar perovskite solar cells. *Nano Energy* **2015**, *12*, 494–500. [CrossRef]

90. Grancini, G.; Marras, S.; Prato, M.; Giannini, C.; Quarti, C.; De Angelis, F.; De Bastiani, M.; Eperon, G.E.; Snaith, H.J.; Manna, L.; *et al*. The impact of the crystallization processes on the structural and optical properties of hybrid perovskite films for photovoltaics. *J. Phys. Chem. Lett.* **2014**, *5*, 3836–3842. [CrossRef] [PubMed]
91. Pathak, S.; Sepe, A.; Sadhanala, A.; Deschler, F.; Haghighirad, A.; Sakai, N.; Goedel, K.C.; Stranks, S.D.; Noel, N.; Price, M.; *et al*. Atmospheric influence upon crystallization and electronic disorder and its impact on the photophysical properties of organic-inorganic perovskite solar cells. *Acs Nano* **2015**, *9*, 2311–2320. [CrossRef] [PubMed]
92. Yang, S.; Zheng, Y.C.; Hou, Y.; Chen, X.; Chen, Y.; Wang, Y.; Zhao, H.; Yang, H.G. Formation mechanism of freestanding $CH_3NH_3PbI_3$ functional crystals: *In situ* transformation vs dissolution-crystallization. *Chem. Mater.* **2014**, *26*, 6705–6710. [CrossRef]
93. Shkrob, I.A.; Marin, T.W. Charge trapping in photovoltaically active perovskites and related halogenoplumbate compounds. *J. Phys. Chem. Lett* **2014**, *5*, 1066–1071. [CrossRef] [PubMed]
94. Wang, Q.; Yun, J.-H.; Zhang, M.; Chen, H.; Chen, Z.-G.; Wang, L. Insight into the liquid state of organo-lead halide perovskites and their new roles in dye-sensitized solar cells. *J. Mater. Chem A* **2014**, *2*, 10355–10358. [CrossRef]
95. Stamplecoskie, K.G.; Manser, J.S.; Kamat, P.V. Dual nature of the excited state in organic-inorganic lead halide perovskites. *Energ. Environ. Sci.* **2015**, *8*, 208–215. [CrossRef]
96. Park, B.-W.; Philippe, B.; Gustafsson, T.; Sveinbjörnsson, K.; Hagfeldt, A.; Johansson, E.M.J.; Boschloo, G. Enhanced crystallinity in organic-inorganic lead halide perovskites on mesoporous Tio_2 via disorder-order phase transition. *Chem. Mater.* **2014**, *26*, 4466–4471. [CrossRef]
97. Docampo, P.; Hanusch, F.C.; Giesbrecht, N.; Angloher, P.; Ivanova, A.; Bein, T. Influence of the orientation of methylammonium lead iodide perovskite crystals on solar cell performance. *APL Mater.* **2014**, *2*. [CrossRef]
98. Ishii, A.; Jena, A.K.; Miyasaka, T. Fully crystalline perovskite-perylene hybrid photovoltaic cell capable of 1.2 V output with a minimized voltage lossa. *APL Mater.* **2014**, *2*. [CrossRef]
99. Chen, Q.; Zhou, H.; Fang, Y.; Stieg, A.Z.; Song, T.-B.; Wang, H.-H.; Xu, X.; Liu, Y.; Lu, S.; You, J.; *et al*. The optoelectronic role of chlorine in $CH_3NH_3PbI_3$(Cl)-based perovskite solar cells. *Nat. Commun.* **2015**, *6*. [CrossRef] [PubMed]
100. De Quilettes, D.W.; Vorpahl, S.M.; Stranks, S.D.; Nagaoka, H.; Eperon, G.E.; Ziffer, M.E.; Snaith, H.J.; Ginger, D.S. Impact of microstructure on local carrier lifetime in perovskite solar cells. *Science* **2015**, *348*, 683–686. [CrossRef] [PubMed]
101. Stranks, S.D.; Nayak, P.K.; Zhang, W.; Stergiopoulos, T.; Snaith, H.J. Formation of thin films of organic-inorganic perovskites for high-efficiency solar cells. *Angew. Chem. Int. Ed.* **2015**, *54*, 3240–3248. [CrossRef] [PubMed]